JOURNAL OF GEOPHYSICAL RESEARCH: OCEANS, VOL. 118, 422–434, doi:10.1029/2012JC008444, 2013

The response of the Red Sea to a strong wind jet near the Tokar Gap in summer

Ping Zhai,[1] and Amy Bower[2]

Received 17 August 2012; revised 19 November 2012; accepted 20 November 2012; published 31 January 2013.

[1] Remote sensing and in situ observations are used to investigate the ocean response to the Tokar Wind Jet in the Red Sea. The wind jet blows down the atmospheric pressure gradient through the Tokar Gap on the Sudanese coast, at about 19°N, during the summer monsoon season. It disturbs the prevailing along-sea (southeastward) winds with strong cross-sea (northeastward) winds that can last from days to weeks and reach amplitudes of 20–25 m/s. By comparing scatterometer winds with along-track and gridded sea level anomaly observations, it is observed that an intense dipolar eddy spins up in response to the wind jet. The eddy pair has a horizontal scale of 140 km. Maximum ocean surface velocities can reach 1 m/s and eddy currents extend more than 100 m into the water column. The eddy currents appear to cover the width of the sea, providing a pathway for rapid transport of marine organisms and other drifting material from one coast to the other. Interannual variability in the strength of the dipole is closely matched with variability in the strength of the wind jet. The dipole is observed to be quasi-stationary, although there is some evidence for slow eastward propagation in an idealized numerical model. Simulation of the dipole in an idealized high-resolution numerical model suggests that this is the result of self-advection.

Citation: Zhai, P., and A. S. Bower (2013), The response of the Red Sea to a strong wind jet near the Tokar Gap in summer, *J. Geophys. Res. Oceans*, *118*, 422–434, doi:10.1029/2012JC008444.

1. Introduction

[2] The Red Sea is a long and narrow basin that is located between Africa and Asia (Figure 1). It extends from 12.5°N to 30°N, a distance of about 2250 km, and is about 280 km wide on average. The average depth is about 490 m, but a rift running down the axis is, in some places, deeper than 2000 m. The Red Sea is connected to the Indian Ocean through the strait of Bab el Mandeb, and to the Mediterranean through the Suez Canal. At about 28°N, the Red Sea splits into the Gulf of Suez and Gulf of Aqaba. At the southern end (about 12°N), the Red Sea has a minimum width of 25 km at the strait of Bab el Mandeb. At 13.7°N, slightly north of the strait of Bab el Mandeb, there is a shallow sill with a greatest depth of 137 m—Hanish Sill [*Werner and Lange*, 1975].

[3] Wind and buoyancy forcing are two mechanisms that drive the Red Sea circulation. The climatological mean surface winds in the Red Sea are mainly along the axis of the basin due to the high mountain ranges on both sides [*Patzert*, 1974]. Winds in the southern part are influenced by the Indian Monsoon. North of 18–19°N, the winds blows southeastward throughout the year. South of 18–19°N, the wind reverses its direction seasonally from north-northwestward in winter to southeastward in summer [*Pedgley*, 1974; *Patzert*, 1974].

[4] *Pedgley* [1974] identified a gap in the high orography on the west coast of the Red Sea near 19°N, which is called the Tokar Gap. *Jiang et al*. [2009] pointed out that there is a strong zonal wind jet that blows across the Red Sea through the Tokar Gap. In summer, the wind jet blows out of the Tokar Gap into the Red Sea [*Hickey and Goudie*, 2007]. In winter, the wind jet blows from the Red Sea into the Tokar Gap [*Pedgley*, 1974, Figure 1]. The mean sea level pressure (SLP) and 10 m sea surface wind in August and December 2001 in the vicinity of the Tokar Gap are shown in Figure 2. In August, the SLP on the African coast is higher than in the Red Sea, and the wind blows down the pressure gradient toward the Red Sea as a gravity flow through the Tokar Gap. The width of the wind jet, which is 150–400 km, is much smaller than the first baroclinic Rossby radius of deformation for the atmosphere (approximately 1000 km). In December, the wind converges into the Tokar Gap, and is almost along the isobars, which implies that the wind in winter might be geostrophically balanced in this region.

[5] Some observational and modeling studies have concluded that eddies play an important role in the horizontal circulation of the Red Sea. *Morcos* [1970] inferred surface circulation patterns from temperature and salinity observations taken during 1895–1896 and 1897–1898. The studies depicted a generally cyclonic circulation with a superimposed, but unresolved, eddy field. *Morcos and Soliman* [1972] depicted a series of mainly cyclonic eddies and an anticyclone centered

[1]MIT-WHOI Joint Program in Physical Oceanography, Woods Hole Oceanographic Institution, Woods Hole, Massachusetts, USA.
[2]Department of Physical Oceanography, Woods Hole Oceanographic Institution, Woods Hole, Massachusetts, USA.

Corresponding author: P. Zhai, 266 Woods Hole Road, Woods Hole Oceanographic Institution MS21, Woods Hole, MA 02540, USA. (pzhai@whoi.edu)

2169-9275/13/2012JC008444

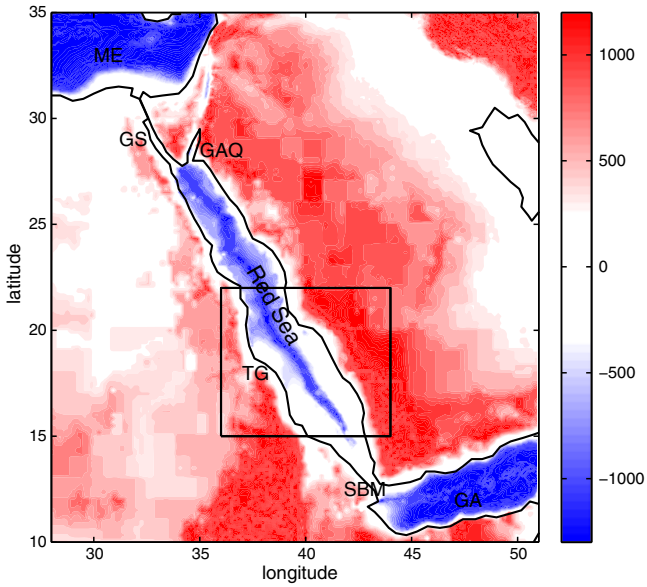

Figure 1. A Red Sea topographic map. The colors are the elevation of the topography (unit: m). The locations of Gulf of Aqaba (GAQ), Gulf of Suez (GS), Gulf of Aden (GA), Mediterranean Sea (ME), Tokar Gap (TG), Strait of Bab el Mandeb (SBM) are shown. The mean Sea Level Pressure (SLP) and 10 m wind in the box (36–44°E and 15–22°N) are plotted in Figure 2.

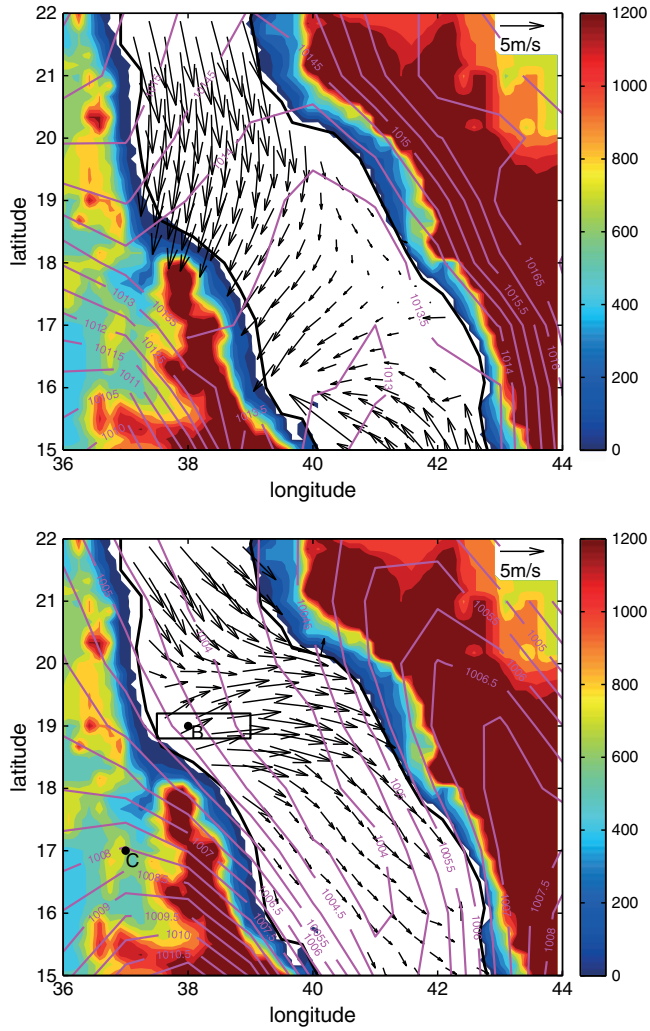

Figure 2. Mean SLP (contour) and 10 m wind in January (upper panel) and August (lower panel) 2001. SLP is from NCEP FNL Operational Model Global Tropospheric Analyses; 10 m wind is from QuikSCAT; the colors are topography from etopo05 (unit: m). The Tokar Gap is located between points B and C.

near 23°N. The hydrographic surveys during the period from 1982 to 1987 revealed that the circulation of the Red Sea was composed of a series of gyres [*Quadfasel and Baudner*, 1993]. *Sofianos and Johns* [2007] demonstrate by using shipboard acoustic Doppler current profiler (ADCP) data from an along-axis cruise track that there is a strong dipole at 19°N near the Tokar Gap with a cyclonic eddy in the north and an anticyclonic eddy in the south.

[6] Eddies in the Red Sea may have important impacts on biological productivity and distributions. Thermocline uplift in the center of the cyclonic eddy may bring the cold water and nutrients from the deep water to the surface layer of the Red Sea, which is generally oligotrophic. This could increase the productivity in that region. In addition, the eddies may transport nutrients from the coastal coral reefs into the interior of the Red Sea. In October 2002, a low chl-*a* region centered along 18.5°N appeared where there was an anticyclonic gyre [*Acker et al*., 2008, Figure 8]. From the satellite altimetry data, the eddies in the Red Sea appear to extend from one side of the Red Sea to the other side, which enhances the interaction and communication of the two coasts of the Red Sea. For example, with the speed of 1 m/s, a particle can travel from the west coast to the east coast in 2–3 days. For this and other reasons related to the general circulation of the Red Sea, it is important to understand more about the formation and dynamics of eddies in the Red Sea.

[7] The formation mechanisms for the eddies in the Red Sea are still uncertain. *Clifford et al.* [1997] pointed out that the formation of eddies in the Red Sea strongly depends on the wind direction. They proposed that there would be more eddies in the Red Sea when the wind has a cross-basin component. There are strong mountain gap winds in the Gulfs of Tehuantepec, Papagayo, and Panama that blow from the Gulf of Mexico to the eastern Pacific Ocean in Central America in winter. *McCreary et al.* [1989] studied the response of the ocean to the gap winds in this region by using a reduced gravity model. In their numerical simulation, the ocean is driven by a wind jet whose structure is similar to that of the wind jet in the Gulf of Tehuantepec. Two counter-rotating gyres are generated, with a cyclonic eddy east of the wind jet and an anticyclonic eddy west of the wind jet. When Coriolis parameter is changing with latitudes in the numerical simulation, the cyclonic eddy is diminished by entrainment of cool water, while the anticyclonic eddy propagates westward at a speed that is slower than the nondispersive Rossby wave speed [*McCreary et al*., 1989]. Dipoles generated by wind jets in the Philippine Archipelago and South China Sea are also studied by using satellite altimetry data and numerical model output [*Pullen et al*., 2008; *Rypina et al*., 2010; *Wang et al*., 2006, 2008]. A major difference between the Tokar wind jet

and wind jets in central America, Philippine Archipelago and the South China Sea is that there are western and eastern boundaries in the Red Sea, which could block zonal propagation of the dipole.

[8] In the present study, the structure, evolution, and dynamics of the dipolar eddy near the Tokar Gap will be studied, using primarily the QuikSCAT scatterometer wind, the satellite sea level anomaly (SLA), in situ observations and a 1.5-layer model. In section 2, measurements of near sea-surface winds by QuikSCAT from July 1999 to November 2009 are analyzed to investigate the seasonal variation of the wind near the Tokar Gap. The response of the Red Sea to the Tokar Wind Jet in summer is described in section 3 using the satellite SLA and in situ observations from shipboard acoustic Doppler current profiler (SADCP) and conductivity-temperature-depth (CTD). In section 4, a 1.5-layer model is employed to study the water movement forced by an idealized zonal wind jet. The influence of the β effect is examined. Section 5 contains conclusions and a discussion of the results.

2. Satellite Observations of the Wind Jets Near the Tokar Gap in the Red Sea

2.1. Data Description

[9] The QuikSCAT winds analyzed here are produced by Remote Sensing Systems and sponsored by the NASA Ocean Vector Winds Science Team (data used here were downloaded from ftp://ftp.ssmi.com/qscat/). They were calculated using the QSCAT-1 model function (Jet Propulsion Laboratory, 2001). QuikSCAT data products include daily and time-averaged wind data (3 day average, weekly and monthly) at 10 m above the sea surface. The data products used here are 0.25 degree gridded data. The daily data are divided into two maps based on ascending and descending passes.

[10] QuikSCAT wind data in the Red Sea is compared to in situ measurements in Figure 3. Beginning in September 2008, as part of a collaboration to improve understanding of Red Sea circulation and hydrography, the Woods Hole Oceanographic Institution began work with King Abdullah University of Science and Technology to maintain a fully-instrumented air-sea interaction mooring in the eastern Red Sea. The first Woods Hole Oceanographic Institution-King Abdullah University of Science and Technology buoy was deployed on 11 October 2008 at 22.16°N, 38.50°E in about 700 m of water. The wind data were collected from 11 October 2008 to 20 November 2009. The QuikSCAT wind used to compare with the buoy winds is daily QuikSCAT swath data (twice a day, ascending and descending passes), and is interpolated to the buoy location. The hourly buoy winds are interpolated to the QuikSCAT wind time. Since the applicable range that fulfills the QuikSCAT technical mission requirements is 3–30 m/s [*Callahan*, 2006], only wind speeds in this range are considered. The scatter plots of the QuikSCAT versus buoy wind speeds and directions (Figure 3) indicate that QuikSCAT captures the wind speed better than the wind direction. The statistical analysis reveals that the linear correlation coefficient is 0.95 for the wind speed with a mean difference and root mean squared difference of –0.02 m/s and 0.68 m/s, respectively. On the other hand, for the wind direction, the linear correlation coefficient is 0.76 with a mean difference and root mean squared difference of 10.7° and 29.9°. These statistical differences are comparable to those found at other sites [*Satheesan et al.*, 2007; *Pickett et al.*, 2003], confirming that the quality of QuikSCAT winds in the Red Sea is comparable to other locations.

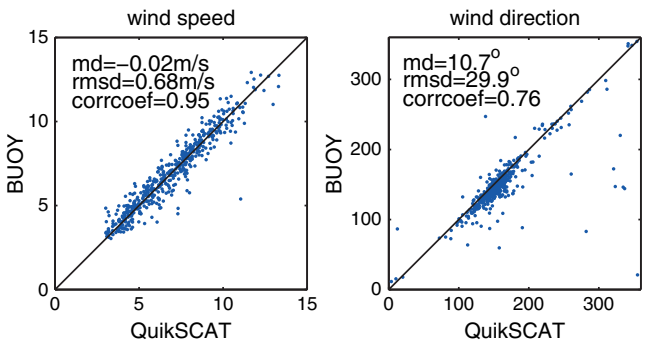

Figure 3. Scatter plot of QuikSCAT versus buoy wind speed and wind direction during the period of October 2008 to November 2009.

2.2. Seasonal and Daily Variability of the Wind Near the Tokar Gap

[11] The climatological mean wind direction inside the Red Sea is along the sea's axis due to high mountain ranges on either side. The mountain gaps on the Red Sea coasts allow for a cross-sea wind component. The Tokar Gap is one of the largest gaps located on the African coast at about 18°N. We plot the wind component along the major jet axis (55° clockwise relative to north) near the Tokar Gap from the QuikSCAT, with positive values representing northeastward wind (Figure 4). The Tokar wind jet is easily identifiable as locally strong (positive) cross-sea winds. The wind near the Tokar Gap has strong seasonal variability. In summer, the wind blows out of the Tokar Gap into the Red Sea; in winter, the wind reverses its direction. The summer Tokar wind jet can last from a few days (year 2006) to a month (year 2001).

[12] It has been previously mentioned that the summer wind jet is driven by the pressure difference between the Tokar Gap and the Red Sea using the Weather Research and Forecast model [*Jiang et al.*, 2009]. To test this relationship using the climate products, we used the National Centers for Environmental Prediction (NCEP) Final (FNL) analysis $1° \times 1°$ gridded SLP field to calculate the pressure difference along the gap axis. As seen in Figure 4 (bottom), the pressure difference along the gap is positive in summer when the wind jet blows northeastward (i.e., the wind is blowing down the pressure gradient). However, the pressure difference is negative in winter when the "convergent wind" blows southwestward into the gap. The maximum SLP difference along the Tokar Gap is about 4 hPa in summer, while negative maximum SLP difference in winter is smaller, less than 2 hPa. However, the amplitudes of the wind in summer and winter do not differ that much. The contours of SLP are more closely spaced in summer than in winter according to Figure 2.

[13] Away from the coast, at a distance of approximately 100 km, the wind jet turns clockwise. The anticyclonic turning of the Tokar Wind Jet might be due to the super-position of the NNW prevailing wind in the Red Sea in summer. In winter, the NNW wind north of the Tokar Gap, and the SSE wind in the south converge into the Tokar Gap. The wind is almost

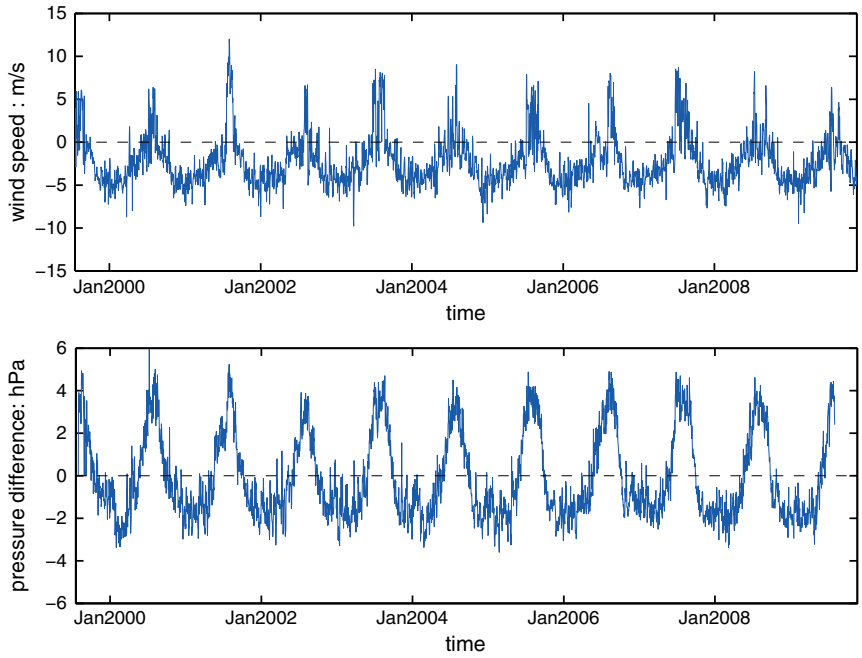

Figure 4. (top) Time series of the 10 m wind component along the major Tokar Wind Jet axis, which is 55° clockwise relative to the north. The wind is averaged in the box marked in the lower panel of Figure 2 (Tokar Wind Jet speed). (bottom) Time series of the 1°-gridded NCEP FNL SLP difference along the gap ($SLP_C - SLP_B$). The locations of the two points are marked as black dots in Figure 2.

parallel to the isobars with high SLP on the right-hand side, which indicates that the wind inside the Red Sea is mainly geostrophically balanced. The geostrophic wind speed is about 8 m/s according to the SLP distribution near the Tokar Gap. Therefore, the mechanisms of the wind near the Tokar Gap in summer and winter might be different. The summer wind jet might be directly driven by the pressure gradient while the winter "convergent wind" might be mostly geostrophically balanced (Figures 3 and 4).

[14] Based on results from an application of the Weather Research and Forecast model to the Red Sea region, which is initialized daily with 1° NCEP FNL, *Jiang et al.* [2009] concluded that the Tokar Wind Jet has strong diurnal variability due to the opposite cross-shore temperature contrast during the day (generating westward sea breezes) and at night (generating eastward land breezes). Therefore, the summer Tokar Wind Jet is stronger in the early morning than in the evening during the summer. The time series of the offshore wind speed from QuikSCAT daily winds near the Tokar Gap in August 2008 confirms the daily cycle of the Tokar Wind Jet (Figure 5).

3. The Response of the Red Sea to the Tokar Wind Jet

3.1. Data Description-Satellite SLA

[15] Satellite altimetry can measure the sea surface height. Mesoscale eddies in the ocean can be detected by their SLA. For example, at latitude 20°N, with a velocity of 0.5 m/s and radius 100 km, the sea level difference between the edge and the center of the eddy is about 25 cm, according to geostrophic balance.

[16] The satellite SLA data used here are computed with respect to the CLS01 mean sea surface height (CLS01 MSS). CLS, Collecte Localisation Satellites, is a subsidiary of the French Space Agency, French Research Institution for exploration of the sea and several French financial institutions [http://www.cls.fr/html/cls/points_cles_en.html]. The CLS01 MSS is computed from 7 years of Topex/Poseidon mean profile (1993–1999), 5 years of ERS-1/2 mean profile (1993–1999), 2 years of Geosat mean profile (1987–1988) and ERS-1 geodetic data [*Hernandez and Schaeffer*, 2001].

[17] The satellite TOPEX/Poseidon was launched on 10 August 1992. It measured the sea surface height every 10 days with an RMS accuracy of 5 cm [*Fu et al.*, 1994]. In the following years, several other altimetry satellites were launched. The repeat periods of GFO (Geosat Follow-On), ERS-1/2, Jason-1/2 and Envisat are 17, 35, 10, and 35 days, respectively. Combining the data of all available satellites, AVISO provides the merged SLA (http://www.aviso.oceanobs.com/en/data/data-access-services/opendap/opendap-sla-products/index.html), which is mapped on a regular 0.25° grid every 7 days. The resolution of the gridded SLA is about

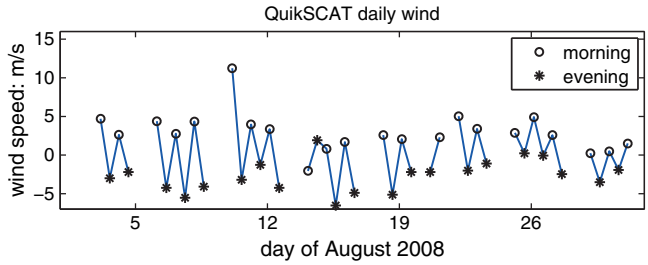

Figure 5. Time series of offshore wind speed from QuikSCAT daily winds near the Tokar Gap averaged in the box in Figure 2. The offshore direction is 55° clockwise relative to the north.

2° in latitude and longitude [*Ducet et al.*, 2000]. The merged SLA data have lower mapping errors and better spatial coverage than would data from one satellite alone [*Ducet et al.*, 2000]. It is important to point out that the data used here are anomalies since the mean dynamic topography is not well-measured in the Red Sea.

[18] The satellite along-track and gridded SLA have been used previously to reveal some features of sea level variability in the Red Sea. *Cromwell and Smeed* [1998] analyzed SLA at (41°E, 17.3°N) and (42°E, 15°N) from 1992 to 1997, and pointed out that the SLA in the southern Red Sea has an annual cycle with amplitude of 18 cm and reaches a maximum in winter.

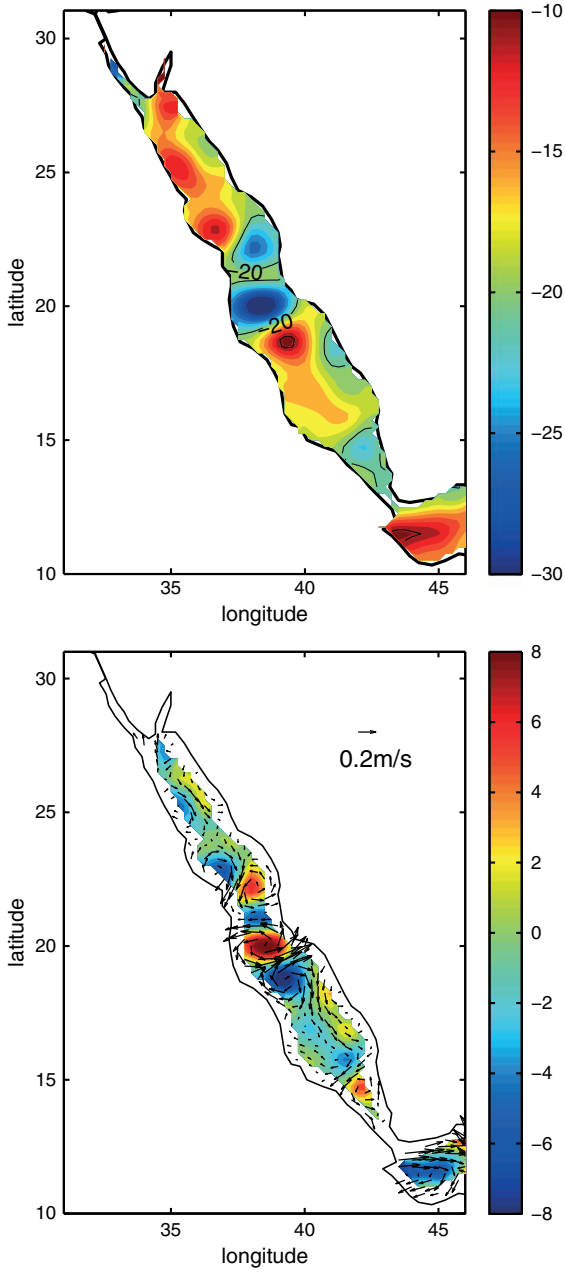

Figure 6. (top) Mean SLA (unit: cm) in August 2001. (bottom) Mean surface geostrophic current anomaly calculated from the SLA and the relative vorticity (unit: 10^{-6} s^{-1}) in August 2001.

3.2. The Dipole Near the Tokar Gap in Summer Observed From Satellite SLA

[19] The satellite altimetry reveals that there are many eddies in the Red Sea throughout the year, that often appear in pairs. The most obvious pair of eddies exists near the Tokar Gap near 19°N in July and/or August. The mean SLA in August 2001 is plotted in Figure 6. It shows that north of 19°N near the Tokar Gap, there is a low SLA center, and south of 19°N, there is a high SLA center. Since the mean dynamic topography is unknown for the Red Sea, only the surface geostrophic current anomaly (eddy geostrophic current) can be calculated. These two counter-rotating eddies of approximately 70 km in radius have basin wide horizontal scale. The gridded SLA product, which has some inherent spatial smoothing, may smear small-scale features.

[20] Figure 7 presents the velocity measured on 13 August 2001 at 22 m depth, obtained with a SADCP [*Sofianos and Johns*, 2007]. The geostrophic surface current anomaly calculated from GFO along-track SLA on 17 August 2001 agrees well with the in situ observations both in direction and in magnitude, which indicates that the along-track satellite data are reliable for studying the dipole. The velocity observations from the SADCP and along-track SLA indicate that azimuthal speeds of the dipole can reach 1 m/s (Figure 7). The geostrophic velocity calculated from the gridded merged SLA typically has a smaller magnitude than that from the along track SLA (Figure 8), as expected [*Ducet et al.*, 2000]. The resolution of the gridded merged SLA is about 2° in the Red Sea [*Ducet et al.*, 2000], which almost covers the whole width of the basin. Although the merged product

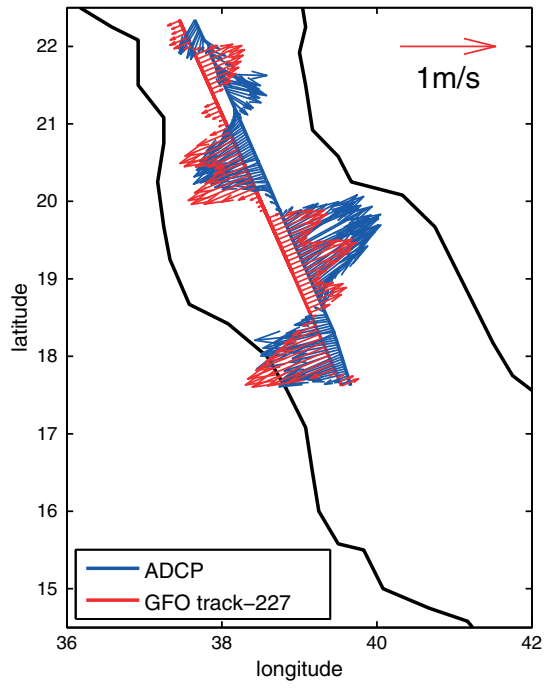

Figure 7. ADCP velocity from in situ observation at 22 m depth and geostrophic current calculated from GFO along track SLA. The in situ data were obtained on 13 August 2001, and the GFO track-227 passed the Red Sea on 17 August 2001. The ADCP data were kindly provided by S. Sofianos.

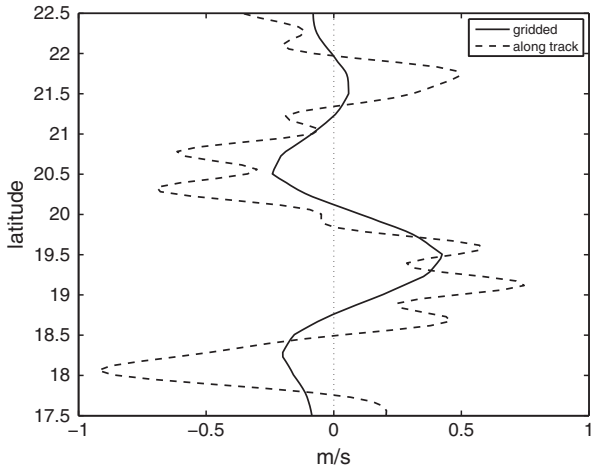

Figure 8. The geostrophic velocity calculated from the GFO along track SLA is the same as in Figure 7. The gridded geostrophic velocity is calculated from merged SLA on 15 August 2001 and then interpolated onto the GFO track-227.

underestimates the strength of the dipole, the comparison between the in situ observation and merged SLA indicates that the merged SLA is still useful for identifying the eddies' evolution because of its consistency in time and space, even though its amplitude is likely underestimated.

[21] The evolution of SLA from late July 2001 to August 2001, highlighting the evolution of cyclonic/anticyclonic eddies near the Tokar Gap in summer, is presented in Figure 9. On 25 July the dipole started to develop. It reached maximum strength on 15 August 2001. At the end of August, the dipole became weaker, and it completely disappeared in winter. What should be mentioned here is that the gridded SLA fields are based on along-track data from ± 15 days. Therefore, it is not possible to investigate the formation of the dipole, estimated to have a spin-up time of about a day (see below), using the gridded SLA.

[22] The QuikSCAT wind stress and the wind stress curl are plotted in Figure 10, for the same time period as in Figure 9. Before 20 July, the wind in the Red Sea was blowing along the Red Sea axis toward the southeast. Starting on 20 July, the wind jet through the Tokar Gap blew almost directly offshore. The wind jet continued for one month and stopped on 22 August 2001. The wind jet has regions of positive and negative wind stress curl on either side of the jet maximum. This causes Ekman convergence and divergence in the upper ocean. The Ekman pumping rate, $w_E = curl(\vec{\tau})/(\rho f)$, has the same sign as the wind stress curl. With Ekman convergence/pumping, the thermocline is depressed, resulting in a

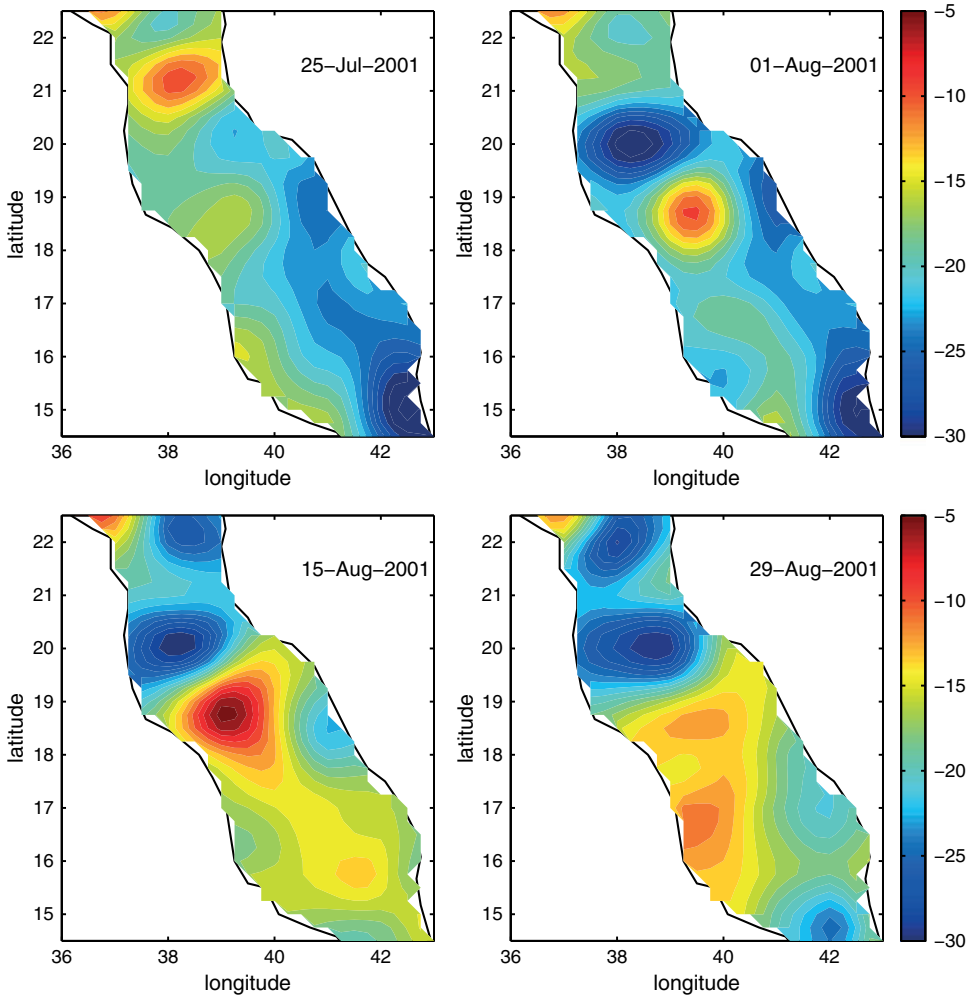

Figure 9. Sequence of the SLA (cm) during 25 July 2001 to 29 August 2001.

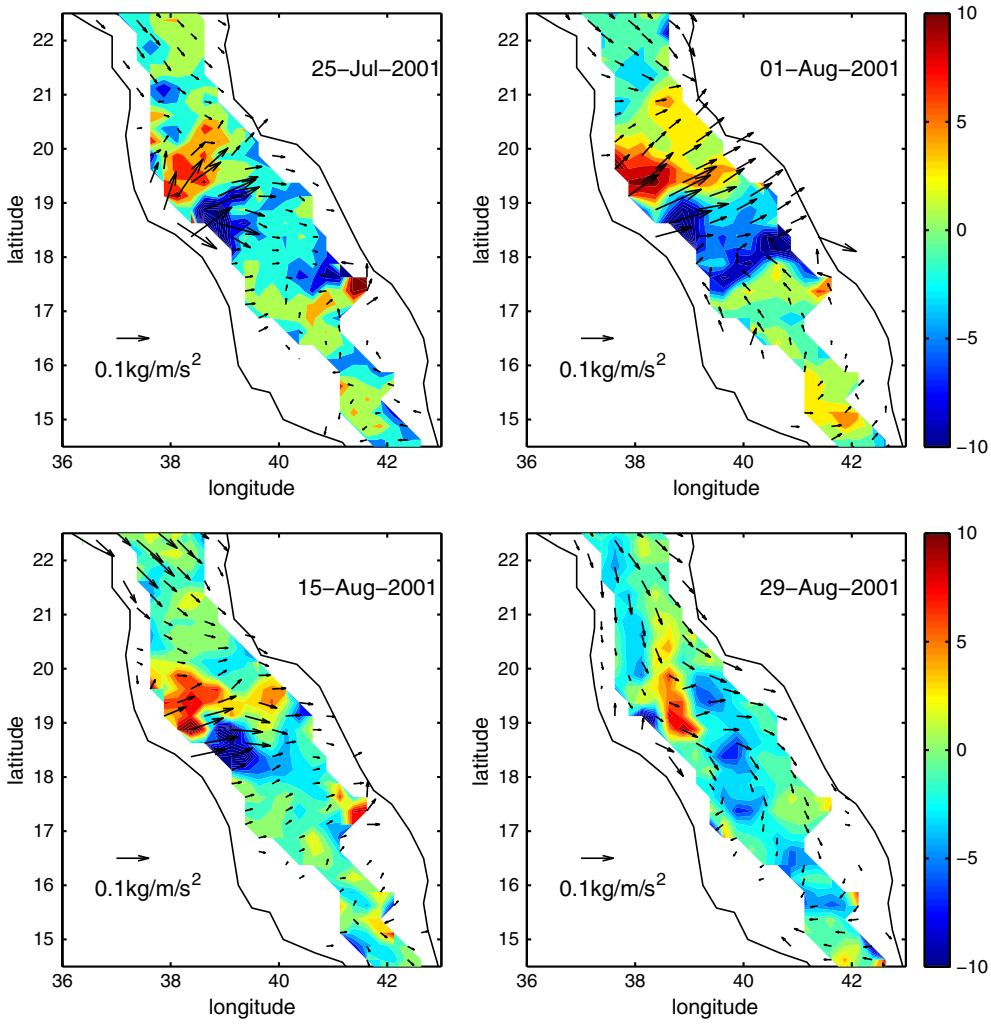

Figure 10. Sequence of the QuikSCAT wind stress and the wind stress curl (unit: 10^{-7} N/m^3) from 25 July 2001 to 29 August 2001.

thicker layer of warm water, which is indicated by a high SLA. Because of geostrophic adjustment, a cyclonic eddy develops with negative SLA and anticyclonic eddy with positive SLA. Thus, the wind jet generates a dipole composed of two eddies rotating in opposite directions. A classical example of dipole generation by mountain gap winds was described by *McCreary et al.* [1989].

[23] According to the QuikSCAT observations, the Tokar Wind Jet formed on 20 July 2001. The spin-up time in the stratified ocean can be estimated from [*Walin*, 1969]

$$T = \frac{1}{Bu^{1/2}} \frac{H}{\delta_e f}, \tag{1}$$

[24] where $Bu = 4N^2H^2/(f^2L^2)$ is the Burger number, N is Brunt-Väisälä frequency, L is the horizontal scale of the wind jet, R_d is the Rossby radius of deformation, H is the water depth, $\delta_e = \sqrt{2A_V/f}$ is the Ekman layer depth, A_V is vertical viscosity. Since no exact value for the diffusivity is available, an empirical formula, $\delta_e = \gamma u_{*\,\mathrm{wind}}/f$, is used to determine the Ekman layer depth. Here $\gamma = 0.25 \sim 0.4$ is an empirical constant, which is determined from observations [*Coleman et al.*, 1990; *Price and Sundermeyer*, 1999], $u_{*\,\mathrm{wind}} = sqrt(\tau/\rho)$ is the friction velocity defined by wind stress and the water density. The horizontal scale of the Tokar Wind Jet is about 90 km. R_d is 30 km in the Tokar Wind Jet region as described in section 3.3. At the center of the cyclonic/anticyclonic eddy, the water depth is about 2000 m. If we choose $H = 2000$ m, $\tau = 0.1$ N/m^2, $\rho = 1025$ kg/m^3, $N = 0.01$ s^{-1}, the spin-up time is about 0.7–1 days. After the wind jet stops, the dipole is observed to dissipate in about one month. For example, in 2003, the Tokar Wind Jet diminished on 250August but the dipole continued active until 24 September.

[25] The strength of the dipole near the Tokar Gap appears to be related to the strength of the summer Tokar Wind Jet. The strength of the dipole agrees well with the Tokar Wind Jet speed in August from 2000 to 2009, except in 2006 (Figure 11). The inconsistency in 2006 might be because of a satellite sampling issue. The maps of satellite ground tracks that passed by the Red Sea in August 2003 and 2006 indicate that there are fewer satellite tracks passing by the Red Sea in August 2006 than in August 2003 (Figure 13). Therefore, the satellite data may not contain enough information to resolve the strength of the dipole in 2006. A regression map of the strength of the

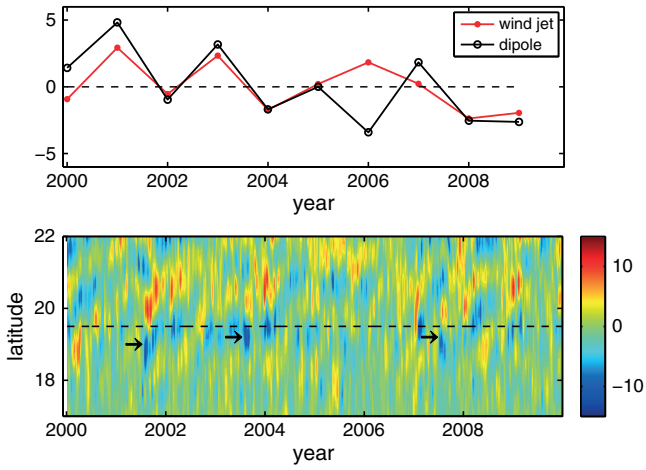

Figure 11. (top) The August anomalies of relative vorticity at the center of the cyclonic eddy of the dipole (black line with open circle, $10^{-6}\,s^{-1}$) and the Tokar Wind Jet speed (red line with dot, m/s, the definition of Tokar Wind Jet speed is the same as Figure 4.) from 2000 to 2009. The mean values averaged from 2000 to 2009 are subtracted to get the anomalies. The mean values are $4.6 \times 10^{-6}\,s^{-1}$ and 2.0 m/s. (bottom) Hovmuller diagram for relative vorticity ($10^{-6}\,s^{-1}$) along the central axis of the Red Sea. The dashed line is the approximate location of the Tokar Gap. The three arrows indicate the strong dipole events in 2001, 2003, and 2007.

cyclonic eddy and the wind speed in the gap direction (55° clockwise relative to north) (Figure 12) indicates the area over which the relative vorticity of the surface currents is correlated with the Tokar Jet.

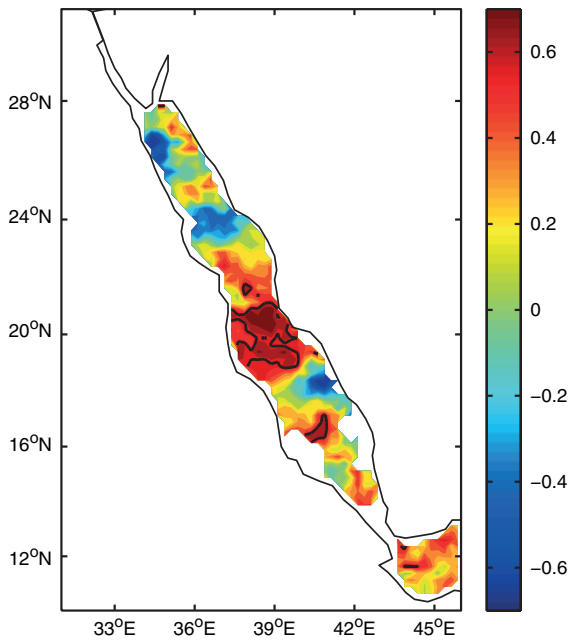

Figure 12. Regression map of strength of the cyclonic eddy (the relative vorticity at the center of the cyclonic eddy, as defined in Figure 11) and the wind speed in the direction of 55° clockwise relative to the north in the Red Sea. The black thick line is the contour of 0.6 correlation coefficient.

3.3. The Horizontal and Vertical Structure of the Dipole

[26] Up to this point, we have focused on surface expressions of the dipole near the Tokar Gap. There is in situ observational evidence that the eddies extend below the sea surface. As discussed above, *Sofianos and Johns* [2007] conducted an along-axis hydrographic and SADCP section in August 2001, which coincided with a strong dipole event. The SADCP observations revealed that the dipole near the Tokar Gap extended to 130 m depth.

[27] Figure 14 shows three eastward velocity profiles on 13 August 2001 measured by using SADCP. The two profiles with negative surface velocity are on two sides of the dipole. The profile with positive surface velocity is in the middle of the dipole, the boundary between the anticyclonic and cyclonic eddies. The velocity profiles suggest that the strength of the dipole decreases rapidly with depth, with a baroclinic structure confined in the upper 130 m. The temperature and salinity profiles of six CTD stations, which were obtained on 12–14 August 2001, are presented in Figure 16. The temperature profiles indicate that the thermocline depth is about 70 m on average with the maximum value at station 48. Both the isotherms and isohalines under the anticyclonic eddy were depressed. In Figure 16, the thermocline depth at station 48, which is close to the center of the anticyclonic eddy, is 40 m lower than that at station 47. According to Figure 16, the density difference between the upper and the lower ocean is about 3 kg/m^3. Taking 1025 kg/m^3 as the average density, the surface rise at the center of the anticyclonic eddy is predicted to be $40 * 3/1025 = 12$ cm, which is in accordance with the satellite observation (Figure 15). In Figure 15, the SLA difference between stations 47 and 48 is about 10 cm in gridded SLA on 8 August 2001. The SLA difference between stations 46 and 47 is about 4 cm, which indicates that the thermocline depth difference should be 13 m. However, the thermocline at station 46 is not uplifted as expected. The depressed thermocline and the raised sea surface at the center of the anticyclonic eddy, together with the horizontal velocity profiles suggest that the vertical structure of the dipole may be well-represented by the first baroclinic mode (Figure 16).

[28] In order to calculate the first baroclinic Rossby radius of deformation, the vertical mode decomposition method is applied on the vertical structure governed by the equation

$$\frac{d}{dz}\left(\frac{1}{N^2(z)}\frac{dF}{dz}\right) + \gamma^2 F(z) = 0, \qquad (2)$$

where F is the vertical structure of horizontal velocity, N^2 is the Brunt-Väisälä frequency, subject to boundary conditions $dF/dz = 0$ at both the surface and bottom, the solutions of equation (2) are the modes $F_n(z)$, γ_n, $0 \le n \le \infty$, γ_n being an eigenvalue. Equation (2) is solved by using finite difference. The physical meaning of γ_n is the inverse of the gravity wave speed of different modes. The zeroth mode is the barotropic mode with a constant vertical structure $F(z)$, the nth mode represents the nth baroclinic mode and $F(z)$ has n zero-crossings. The barotropic and the first three baroclinic vertical structure modes at station 47 are presented in Figure 17. The zero-crossing of the first baroclinic mode is at 200 m, which corresponds to station 47's thermocline depth of about 150 m.

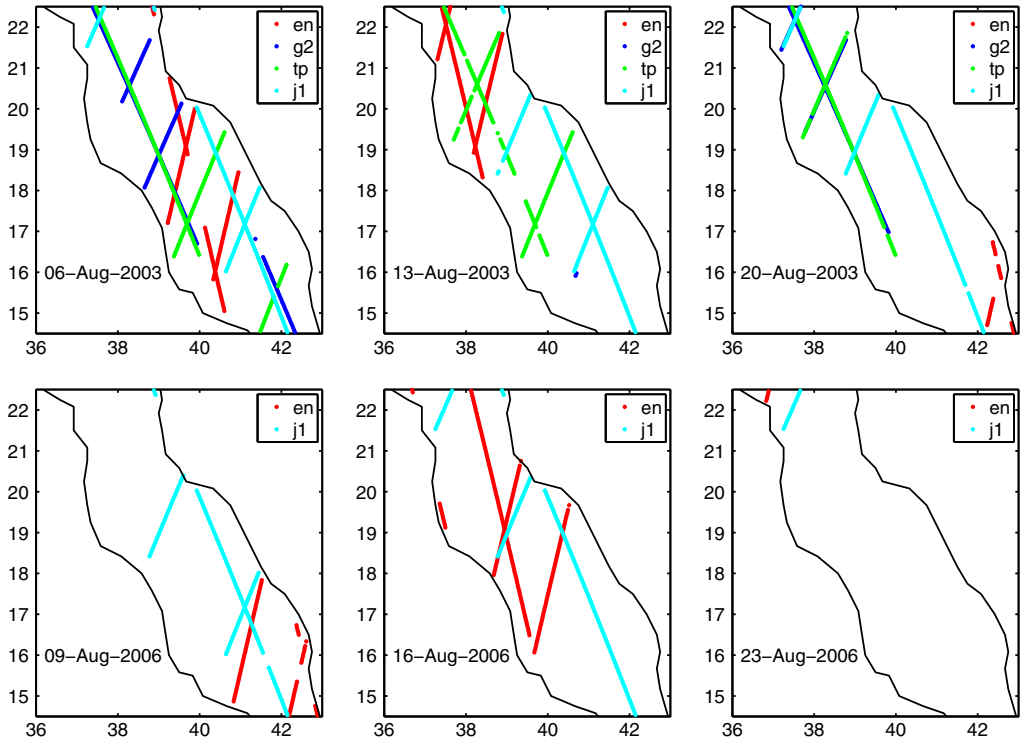

Figure 13. Satellite ground tracks passing by the Red Sea during ±3 days of the dates shown in the figure. en-Envisat, g2-GFO, tp-TOPEX/Poseidon, j1-Jason1.

[29] The first baroclinic Rossby radius of deformation can be calculated from $R_{d1} = 1/(f\gamma_1)$. The deformation radius calculated from the mean temperature and salinity profiles of stations 46, 47, and 48 is 30 km (Table 1). The eddies of the dipole are about 70 km in radius, which is twice that of the first baroclinic Rossby radius of deformation.

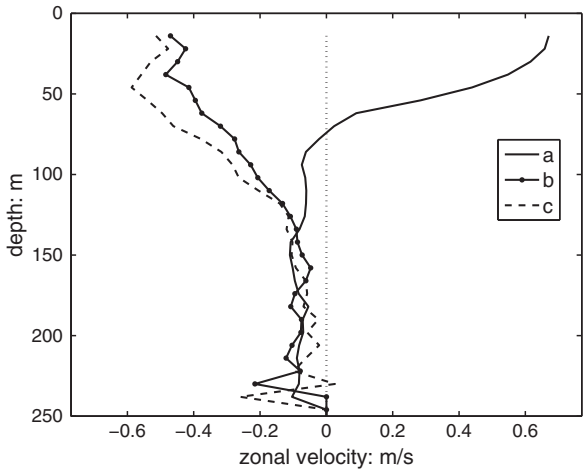

Figure 14. ADCP eastward velocity profiles near the center and edges of the dipole. The location of the velocity profiles are plotted in Figure 15. The solid line represents the velocity profile in the middle of the dipole which consists of two eddies rotating in opposite directions. The dashed line represents the velocity profile on the south side of the anticyclonic eddy and the dotted line is on the north side of the cyclonic eddy.

4. Idealized Simulation Using a 1.5-layer Model

[30] The spatial resolution of the satellite altimetry SLA is about 200 km in the Red Sea, which is not sufficient to study the structure and evolution of the dipole near the Tokar Gap. Therefore, a numerical model is used to understand the mechanism of the dipole. In section 3, it was proved that the vertical structure of the dipole is well represented by the first baroclinic mode. The vertical mode decomposition of the horizontal velocity tells us that the velocity in the lower layer

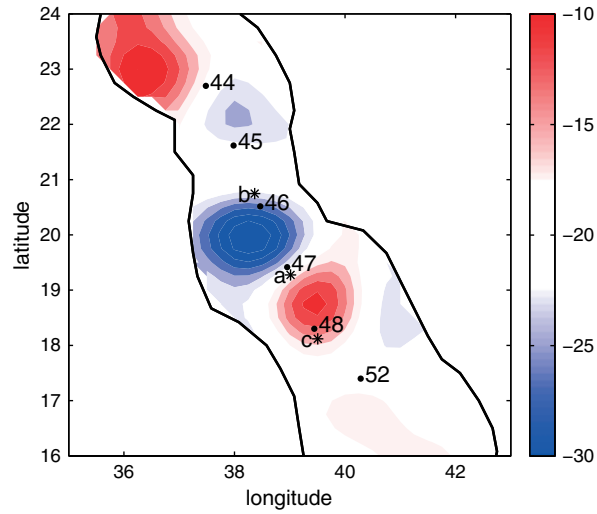

Figure 15. Black dots indicate the location of the CTD stations, black stars are the location of the velocity profiles in Figure 14; the background is SLA (unit: cm) on 8 August 2001.

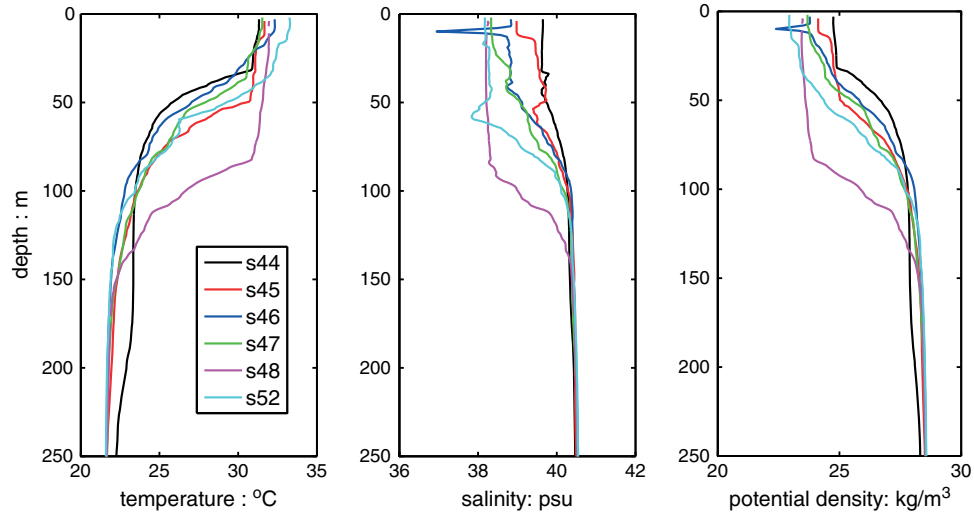

Figure 16. The potential density, temperature, and salinity profiles of six stations in the upper 250 m. The locations of CTD stations are shown in Figure 15. (The data were kindly provided by S. Sofianos.)

is about 6% of the velocity in the upper layer for the first baroclinic mode, which indicates that the movement in the lower layer is negligible compared with the upper layer. Therefore, a 1.5-layer model is appropriate in this study to investigate the dynamics of the dipole driven by the wind jet.

4.1. Model Description

[31] In the 1.5-layer model, also called the reduced gravity model, a single active layer with density of ρ_1 overlays a motionless layer of infinite thickness with different density ρ_2. The momentum and continuity equations for the 1.5-layer model are

$$\begin{aligned} u_t + uu_x + vu_y - fv &= -g'h_x + \frac{\tau^x}{\rho_1 h} + A\nabla^2 u \\ v_t + uv_x + vv_y + fu &= -g'h_y + \frac{\tau^y}{\rho_1 h} + A\nabla^2 v \\ h_t + hu_x + hv_y &= 0 \end{aligned} \tag{3}$$

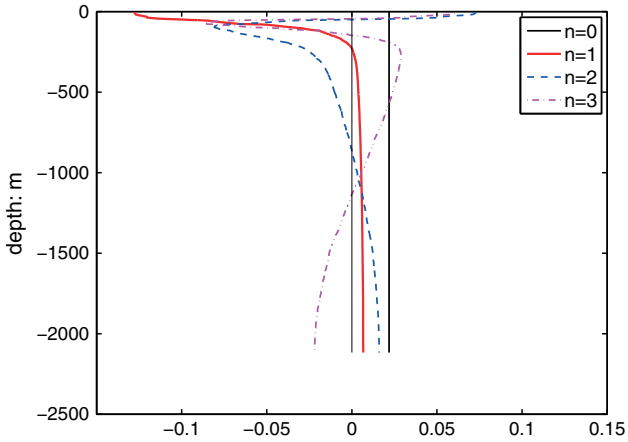

Figure 17. Vertical structure of horizontal velocity for modes 0 to 3 at station 47.

where h is the layer thickness, (u,v) are the horizontal velocity, $f = 2\Omega \sin\varphi$ is the Coriolis parameter and changes with latitude φ, $g' = g(\rho_2 - \rho_1)/\rho_1$ is the reduced gravity, (τ^x,τ^y) are the wind stress components, A is the coefficient of the lateral viscosity. The subscripts t, x, and y indicate partial derivatives. The model used here is the same as *Yang and Price* [2007], except that wind forcing is added with no diapycnal mass flux. The numerical code of the 1.5-layer model was kindly provided by J. Yang. In this model, the pressure gradient in the second layer vanishes and the sea level η is related to the layer thickness h by

$$\eta = \frac{\rho_2 - \rho_1}{\rho_1}(h - H) \tag{4}$$

where H is the initial thickness of the upper layer. In the 1.5-layer model, baroclinic instability cannot occur.

[32] According to in situ observations, the dipole can reach 130 m depth, so H is chosen to be 100 m. The density of the upper layer and lower layer are 1025 kg/m^3 and 1028 kg/m^3, respectively, according to the hydrographic data measured in 2001 provided by S. Sofianos. The lateral viscosity is chosen to be 1000 m^2/s. The model ocean has a rectangular basin in the domain (10 ~ 31°N, 37 ~ 40.5°E). The time interval of integration is 108 s. The horizontal grid spacing is 0.1° × 0.1° (about 10 km). The internal Rossby radius of deformation $\sqrt{g'H}/f$ is about 34 km, which is larger than the horizontal grid spacing.

Table 1. The First Baroclinic Mode Rossby Radius of Deformation (R_d) of 6 CTD Stations. The Mean Rossby Radius of Deformation is Calculated From the Mean Stratification of Stations 46, 47, and 48

Station #	44	45	46	47	48	52	Mean
R_d (km)	22	27	26	32	39	38	30

4.2. The Idealized Simulation

[33] The model is forced by wind fields similar to the wind jet near Tokar Gap in the summer. The wind jet is directed offshore as sketched in equation (5).

$$\begin{aligned} \tau^x &= 0.1 \times X(longitude)Y(latitude)T(t) \\ \tau^y &= 0 \\ X(longitude) &= \exp\left[-(longitude - 37.175)^2/3\right] \\ Y(latitude) &= \exp\left[-(latitude - 19.075)^2 \times 1.7\right] \\ T(t) &= 1 - \exp\left(-\frac{t}{100}\right) \end{aligned} \tag{5}$$

[34] In equation (5), $T(t)$ which increases gradually from 0 to 1 with time, is applied to reduce the impact of inertial oscillations. The horizontal structure of the idealized wind jet is sketched in Figure 18. The lower panel of Figure 18 is the comparison between the idealized wind jet and the mean Tokar Wind Jet in August 2001. The idealized wind jet has the same magnitude and spatial scale as the mean Tokar Wind Jet in August 2001. The initial velocity is zero and nonslip boundary conditions are used.

[35] The response of the 1.5-layer model to the steady wind jet is summarized in Figure 19. In this experiment (EXP1), nonlinear advection, β effect and lateral friction are included. When the wind jet is applied, the sea level drops (Figure 19, hour = 8) at the western coast of the basin due to the offshore ageostrophic flow, which is generated from the exponentially increasing wind in the first few days. The ageostrophic current is related to the time evolution of the wind, which was described by *McCreary et al.* [1989]. Because of the Ekman convergence and divergence, the sea level drops on the north of the wind jet axis and rises on the south. The meridional Ekman drift transports water from the north to the south (Figure 19, hour = 32). Due to the geostrophic adjustment, a dipole consisting of two counter-rotating eddies spins up around the sea level dropping center and rising center (Figure 19, day = 8 and 30). As time goes by, the dipole becomes stronger and moves eastward at a speed of approximately 2.1 cm/s.

[36] In order to investigate the impact of the effect of β on the movement of the dipole, another numerical simulation was conducted—EXP2 (without β effect). When the Coriolis parameter f is constant, the dipole moves eastward at a speed of 3.3 cm/s, faster than in EXP1. That is because the effect of β allows for westward propagating Rossby waves, which slows the eastward self-propagating speed of the dipole. The Rossby wave speed

$$c = -\frac{\beta}{k^2 + l^2 + L_d{}^{-2}}, \tag{6}$$

is 1.1 cm/s if we choose the wavelength as 280 km, which is four times the eddy's radius. $R_d = \sqrt{g'H}/f = \sqrt{3 * 9.8/1025 * 100}/f = 34$ km is the internal Rossby deformation radius. The difference of the propagation speed between EXP1 and EXP2 is 1.2 cm/s, very close to the theoretical Rossby wave speed. In EXP3 and EXP4, the density difference and H are 20 kg/m^3 and 200 m respectively, and the Rossby radius of deformation is increased to 124 km. The difference between EXP3 and EXP4 is that f changes with latitude in EXP3 while it is constant in EXP4. The dipole propagates 1.8 cm/s faster zonally in EXP4 than in EXP3. The Rossby wave speed in these two experiments is about 2.0 cm/s. The comparisons between EXP1 and EXP2, EXP3 and EXP4 suggest that the effect of β is to slow the eastward propagation of the dipole. The results of EXP2, 3, and 4 are not shown here.

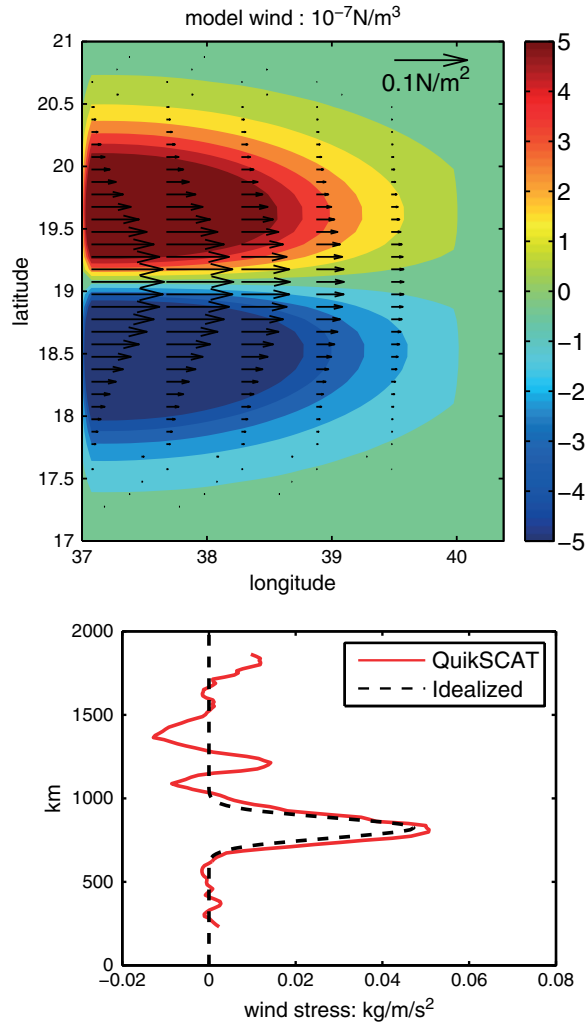

Figure 18. (top) The idealized wind jet and the wind stress curl (10^{-7} N/m^3) used in the 1.5-layer model. (bottom) The offshore direction component of the wind stress along the middle axis of the basin. For the QuikSCAT wind, the offshore direction is 55° clockwise relative to the north; for the wind jet in the idealized model, the offshore direction is eastward.

[37] For simplicity, the model ocean basin used here was oriented north-south, which is different from the Red Sea. If a tilted basin had been used in this model and the wind jet was still perpendicular to the coast, the self-propagation speed of the dipole would not be parallel to the Rossby wave propagation direction. Then the dipole would move northward.

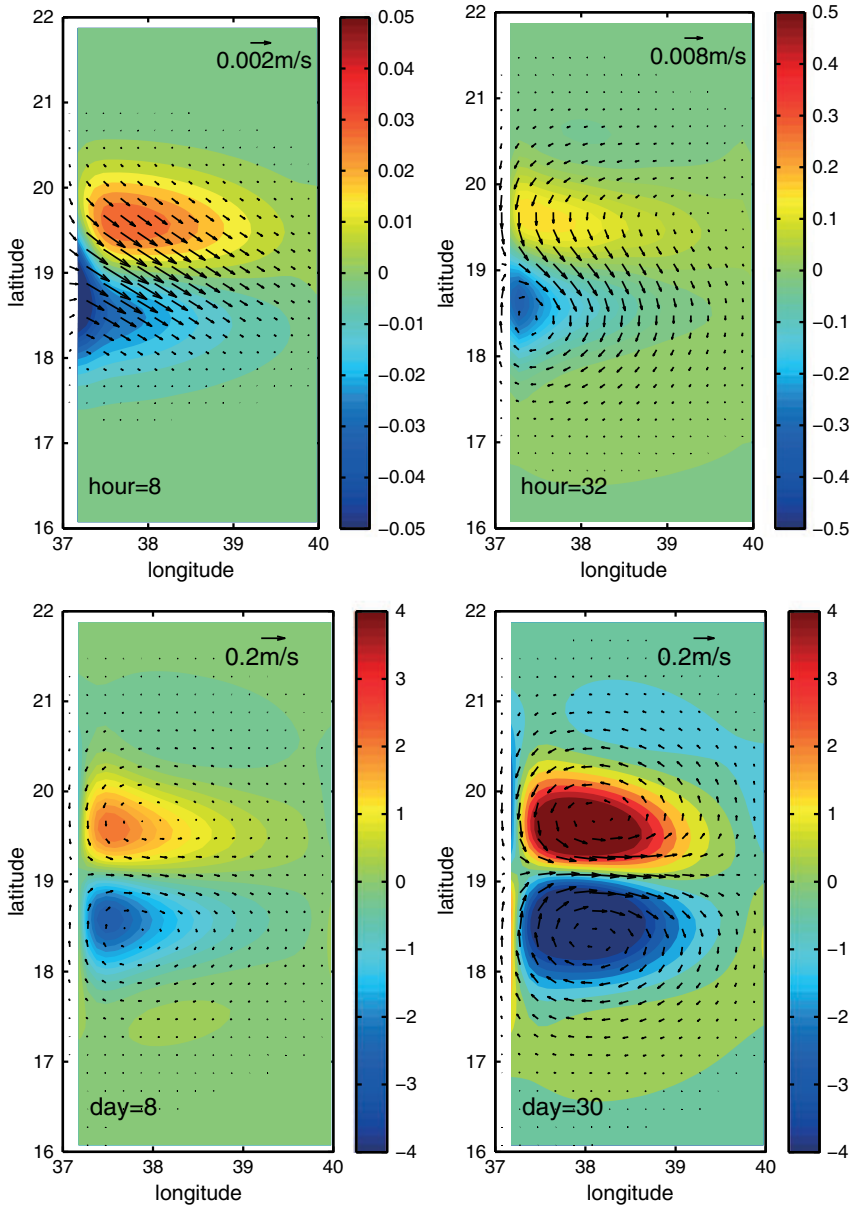

Figure 19. The time evolution of the sea level (unit: cm) and current in the numerical model, which includes nonlinear advection, β effect and lateral friction (EXP1).

5. Conclusions and Discussion

[38] The goals of this study were to describe the seasonal cycle of the Tokar Wind Jet in the Red Sea and to investigate the response of the upper ocean to the jet. QuikSCAT wind data from 1999 to 2009 revealed that in the summer, usually starting in July, the wind blows eastward through the Tokar Gap onto the Red Sea surface down the pressure gradient. The speed of the wind jet can reach 18 m/s based on QuikSCAT records on 12 July 2008, although shipboard observations in 2001 indicate speeds as high as 20–25 m/s (S. Sofianos, personal communication).

[39] Analysis of satellite SLA indicates that after the onset of a summer Tokar Wind Jet event, a dipolar eddy forms, composed of a cyclonic eddy north of the wind jet axis, and an anticyclonic eddy on the south. The strength of the dipole is highly influenced by the strength of the summer Tokar Wind Jet. The in situ observations from *Sofianos and Johns* [2007] confirmed results from SLA analysis indicating that the maximum surface velocity of the dipole can be about 1 m/s. The dipolar circulation is restricted to the upper 130 m according to SADCP velocity, salinity, and temperature profiles. Below 130 m, the flow is much weaker with the velocity smaller than 0.1 m/s. The first baroclinic Rossby radius of deformation is about 30 km in the dipole region, which is smaller than the eddies' radius—70 km.

[40] A 1.5-layer model was used to resolve the dipole generated by the Tokar Gap wind jet in the summer. In response to wind forcing meant to mimic the Tokar jet, the model develops an eddy dipole similar to ones seen in altimetric SLA. After the dipole is generated, it moves eastward due to the self-propagation. Two numerical experiments were designed to determine the influence of the β effect. The results reveal that the effect of β decreases the

eastward self-propagation speed of the dipole by the Rossby wave speed.

[41] The analysis of the observations and numerical model results provide strong evidence that the wind jet is the main mechanism for the generation of the dipole in summer near the Tokar Gap. *McCreary et al*. [1989] used a 1.5-layer model to study the dipole generated by wind jets in the Gulfs of Tehuantepec and Papagayo. The models in their work included a linear model and a nonlinear model with entrainment. The dipole generated by the wind jet propagated westward at a speed close to the linear Rossby wave speed in their linear model. In their nonlinear model, the cyclonic gyre vanished in the end and the anticyclonic gyre propagated westward at a speed faster than the linear Rossby wave speed. *McCreary et al*. [1989] concluded that the difference was due to the nonlinearity. However, in their study, they did not mention the impact of self-propagation of the dipole. In our model, there is both western and eastern boundaries, which influences the zonal propagation of the dipole. It has been proved that the zonal propagation speed of the dipole in our model is the result of the combined effects of eastward self-propagation and westward Rossby wave propagation, and that self-propagation dominates the dipole's zonal movement.

[42] Since there are insufficient observations to determine the background potential vorticity distribution, we cannot rule out baroclinic instability of the mean flow as a possible mechanism for the generation of the dipole. However, the observed correlation between the strength of the summer jet and the dipole, and the ability of the 1.5-layer model forced with an idealized wind jet to simulate the main structure of the dipole, strongly suggest that the wind jet is the main formation mechanism of the dipole. Remaining questions include what causes the interannual variability in the strength of the wind jet. Does the summer jet lead to locally enhanced air-sea fluxes and how important is the dipole to the local ecosystem? Further observational, numerical, and theoretical studies are needed to answer these questions.

[43] **Acknowledgments.** We would like to thank Sarantis Sofianos for providing us the observational CTD and SADCP data used in this study, J. Thomas Farrar for providing us the buoy data, and Jiayan Yang for providing us with the 1.5-layer model code. This work was supported by award USA 00002, KSA 00011 and KSA 00011/02 made by King Abdullah University of Science and Technology (KAUST).

References

Acker, J., G. Leptoukh, S. Shen, T. Zhu, and S. Kempler (2008), Remotely-sensed chlorophyll a observations of the northern Red Sea indicate seasonal variability and influence of coastal reefs, *Journal of marine systems*, *69*, 191–204.

Callahan, P. S. (2006), QuikSCAT Science Data Product User's Manual, Overview and Geophysical Data Products, V3.0, D-18053-RevA, Jet Propulsion Laboratory,Pasadena, California.

Clifford, M., C. Horton, J. Schmitz, and L. H. Kantha (1997), An oceanographic nowcast/forecast system for the Red Sea, *Journal of Geophysical Research-Oceans*, *102* (C11), 25,101–25,122.

Cromwell, D., and D. A. Smeed (1998), Altimetric observations of sea level cycles near the Strait of Bab al Mandab, *Int. J. Remote Sens.*, *19*, 1561–1578.

Coleman, G. N., J. H. Ferziger, and P. R. Spalart (1990), A numerical study of the turbulent Ekman layer, *J. Fluid Mech.*, *213*, 313–348.

Ducet, N., P. Y. Le Traon, and G. Reverdin (2000), Global high-resolution mapping of ocean circulation from TOPEX/Poseidon and ERS-1 and -2, *J. Geophys. Res.*, *105*(C8), 19,477–19,498, doi:10.1029/2000JC900063.

Fu, L.-L., E. J. Christensen, C. A. Yamarone Jr., M. Lefebvre, Y. Menard, M. Dorrer, and P. Escudier (1994), TOPEX/POSEIDON mission overview, *J. Geophys. Res.*, *99*, 24,369–24,381.

Hernandez, F., and P. Schaeffer (2001), The CLS01 mean sea surface: A validation with the GSFC00.1 surface, Tech. Rep., CLS, Ramonville, St Agne, France.

Hickey, B., and A. S. Goudie (2007), The use of TOMS and MODIS to identify dust storm source areas: The Tokar delta (Sudan) and the Seistan basin (south west Asia), In *Geomorphological Variations*, edited by A. S. Goudie and J. Kalvoda, pp. 37– 57, P3K, Prague.

Jet Propulsion Laboratory (2001), SeaWinds on QuikSCAT Level 3: Daily, Gridded Ocean Wind Vectors (JPL SeaWinds Project), Guide Document Version 1.1.

Jiang, H., J. T. Farrar, R. C. Beardsley, R. Chen, and C. Chen (2009), Zonal surface wind jets across the Red Sea due to mountain gap forcing along both sides of the Red Sea, *Geophys. Res. Lett.*, *36*, L19605, doi:10.1029/2009GL040008.

McCreary, J. P., H. S. Lee, and D. B. Enfield (1989), Response of the coastal ocean to strong offshore winds: With application to circulations in the Gulf of Tehuantepec and Papagayo, *J. Mar. Res.*, *47*, 81–109.

Morcos, S. (1970), Physical and chemical oceanography of the Red Sea, *Oceanogr. Mar. Biol.*, *8*, 73–202.

Morcos, S., and G. F. Soliman (1972), Circulation and deep water formation in the northern Red Sea in winter, L'Oceanographie Physique de la Mer Rouge, UNESCO, 91–103.

Patzert, W. C. (1974), Volume and heat transports between the Red Sea and Gulf of Aden, notes on the Red Sea heat budget, In: *L'oceanographie physique de la Mer Rouge*, CNEXO, Paris, pp. 191–201.

Pedgley, D. E. (1974), An outline of the weather and climate of the Red Sea, In: *L'oceanographie physique de la Mer Rouge*, CNEXO, Paris, pp. 9–27.

Pickett, M. H., W. Tang, L. K. Rosenfeld, and C. H. Wash (2003), QuikSCAT satellite comparisons with nearshore buoy wind data off the U.S. west coast, *J. Atmos. Oceanic Technol.*, *20*, 1869–1979.

Price, J. F., and M. A. Sundermeyer (1999), Stratified Ekman layers, *J. Geophys. Res.*, *104*(C9), 20,467–20,494, doi:10.1029/1999JC900164.

Pullen, J., J. D. Doyle, P. May, C. Chavanne, P. Flament, and R. A. Arnone (2008), Monsoon surges trigger oceanic eddy formation and propagation in the lee of the Philippine Islands, *Geophys. Res. Lett.*, *35*, L07604, doi:10.1029/2007GL033109.

Quadfasel, D., and H. Baudner (1993), Gyre-scale circulation cells in the Red-Sea, *Oceanologica Acta*, *16* (3), 221–229.

Rypina, I. I., L. J. Pratt, J. Pullen, J. Levin, and A. Gordon (2010), Chaotic advection in an archipelago, *Journal of Physical Oceanography*, *40*(9), 1988–2006.

Satheesan, K., A. Sarkar, A. Parekh, M. R. Ramesh Kumar, and Y. Kuroda (2007), Comparison of wind data from QuikSCAT and buoys in the Indian Ocean, *Int. J. Remote Sensing*, *10*, 2375–2382.

Sofianos, S. S., and W. E. Johns (2007), Observations of the summer Red Sea circulation, *J. Geophys. Res.*, *112*, C06025, doi:10.1029/2006JC003886.

Walin, G. (1969), Some aspects of time-dependent motion of a stratified rotating fluid, *J. Fluid Mech*, *36*, 289–307.

Wang, G., D. Chen, and J. Su (2006), Generation and life cycle of the dipole in the South China Sea summer circulation, *J. Geophys. Res.*, *111*, C06002, doi:10.1029/2005JC003314.

Werner, F., and K. Lange (1975), A Bathymetric Survey of the Sill Area between the Red Sea and the Gulf of Aden, *Geol. Jahrb. D*, *13*: 125–130.

Yang, J., and J. F. Price (2007), Potential Vorticity Constraint on the Flow between Two Basins, *J. Phys. Oceanogr.*, *37*, 2251–2266, doi:10.1175/JPO3116.1.